

Optics design with longer L^* for the final focus system of Compact Linear Collider 380 GeV

Andrii Pastushenko^{1,2,*}, Rogelio Tomás,¹ and Angeles Faus-Golfe²

¹CERN, 1211 Geneva, Switzerland

²Laboratoire de Physique des 2 Infinies, Irene Joliot-Curie Laboratory IJCLab, CNRS/IN2P3, Université Paris-Saclay, Orsay 91898, France



(Received 10 March 2022; revised 15 June 2023; accepted 30 August 2023; published 26 September 2023)

The Compact Linear Collider (CLIC) plans to start operation at a center-of-mass energy of 380 GeV. This paper reports on various optimizations of the CLIC 380-GeV Final Focus System (FFS). Analytical approximations have been used to guide the numerical optimizations. The first optimization consists of the reduction of the vertical beta function at the interaction point to 70 μm , which is at the limit of the hourglass effect. The second optimization focuses on minimizing the lengths of the final doublet quadrupoles to reduce the chromaticity. The third optimization searched for alternative optics configurations, resulting in the implementation of a novel dispersion profile along the FFS. This alternative optics boosts both total and peak luminosities by 7% and 9%, respectively.

DOI: [10.1103/PhysRevAccelBeams.26.091003](https://doi.org/10.1103/PhysRevAccelBeams.26.091003)

I. INTRODUCTION

The Compact Linear Collider (CLIC) [1] aims to provide lepton collisions up to 3 TeV center-of-mass energy [2]. In the recent update of the CLIC staging strategy [3], the initial stage of the project is foreseen to be 380 GeV. The high total luminosity at the interaction point (IP) is provided by focusing the beams in the beam delivery system (BDS), which is located after the linac, see Fig. 1. Originally, the BDS at 380 GeV was obtained by scaling down the 500-GeV lattice [4]. Beam properties after the acceleration are measured in the diagnostics section. It is followed by the energy collimation section, where the particles with a relative energy offset larger than 1.3% are removed from the beam [5]. The betatron collimation removes the particles with a large transverse amplitude, applying the collimation depth of $15\sigma_x \times 55\sigma_y$ [6]. The final focus system (FFS) is the last section of the BDS and is responsible for the demagnification of the beam to the nanometer level, needed to satisfy the high luminosity requirements at the IP. The final doublet (FD) consists of the last two quadrupoles (QF1 and QD0) upstream of the IP. They strongly reduce the beta functions at the IP to $\beta_x^* = 8 \text{ mm}$ and $\beta_y^* = 100 \mu\text{m}$ (CLIC 380 GeV), see Table I. The FD is also a strong

source of chromaticity at the IP, especially in the vertical plane, approximately given by $\xi_y^* \approx L^*/\beta_y^*$. Here, L^* is the distance between the last quadrupole (QD0) and IP. To cancel the chromatic aberrations at the IP, CLIC uses an FFS design based on the local chromaticity correction scheme [7]. It uses two interleaved sextupoles in the FD to correct the horizontal and vertical chromaticities simultaneously. Figure 2 shows the scheme of the FFS, highlighting the key elements of the lattice.

Following the proposed strategy, all the CLIC energy stages will share the same detector, called CLICdet [8]. It has a total length of 11.4 m, and including the end coil dimension, the half-length of the detector is 5.918 m. These data were used to design the optics of CLIC 3 TeV with QD0 completely outside of the detector [9] with $L^* = 6 \text{ m}$. It was done to exclude the need to shield QD0 with the antisolenoid and to simplify the machine detector interface (MDI). The same strategy was applied to CLIC 380 GeV lattice [10]. The optics with $L^* = 6 \text{ m}$ was obtained by scaling the old version with L^* of 4.3 m (see Table I). The aperture, calculated for such an optics [11], is shown in Fig. 3. In the calculations, the maximum pole tip field in the BDS magnets with exempt of FD quadrupoles, is set to 1.5 T to respect the limitation of the iron saturation [12]. Also, the minimum value of the beampipe radius is set to 15 mm above which the resistive wall effects are considered negligible.

In this paper, we report the optimizations of the FFS optics of CLIC 380 GeV made in several stages. The first optimization consists of reducing the vertical beta function to 70 μm to reach the limit of the hourglass effect [13] and is described in Sec. II. As a second optimization, the FD

*andrii.pastushenko@cern.ch

Published by the American Physical Society under the terms of the [Creative Commons Attribution 4.0 International license](https://creativecommons.org/licenses/by/4.0/). Further distribution of this work must maintain attribution to the author(s) and the published article's title, journal citation, and DOI.

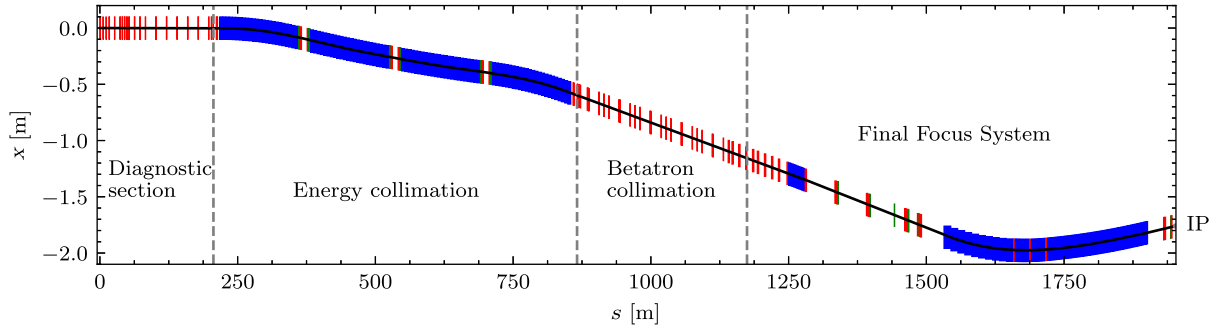


FIG. 1. Layout (view from the top) of the beam delivery system of CLIC at 380 GeV, including dipoles (blue), quadrupoles (red) and sextupoles (green).

quadrupoles have been shortened to reduce the chromaticity. In this case, two optics have been designed, one with a traditional dispersion profile and another with a novel dispersion profile. The optics with the traditional dispersion profile is discussed in Sec. III and the second optics with a novel dispersion profile is described in Sec. IV. Based on these designs and the specification of the collimation section, the aperture for the BDS has been recalculated in Sec. VI.

II. NONLINEAR OPTIMIZATION OF THE OPTICS WITH REDUCED β_y^*

Lepton colliders use flat beams at the IP in order to maximize the luminosity while keeping the beam-beam parameters within certain limits [14]. As a result, both the vertical beam size and beta function are maintained at very small values.

The beta function in the region between the IP and the first quadrupole of the FD, at a distance $s < L^*$ from the IP is given by the following equation:

$$\beta_{x,y}(s) = \beta_{x,y}^* + \frac{s^2}{\beta_{x,y}^*}. \quad (1)$$

When β_y^* is comparable to the bunch length, the beam size varies significantly along the longitudinal range of

TABLE I. Summary table of the key parameters of the scaled FFS for CLIC 380 GeV with $L^* = 6$ m.

FFS length (m)	770
Normalized emittance (IP) $\epsilon_{n,x}/\epsilon_{n,y}$ (nm)	950/30
Beta function (IP) β_x^*/β_y^* (mm)/(mm)	8/0.1
IP beam size σ_x^*/σ_y^* (nm)	144/2.9
Bunch length σ_z (μm)	70
rms energy spread δ_p (%)	0.3
Number of particles in one bunch N ($\times 10^9$)	5.2
Number of bunches in one train N_b	352
Repetition rate f (Hz)	50
Total luminosity \mathcal{L} ($10^{34} \text{ cm}^{-2} \text{ s}^{-1}$)	1.5
Peak luminosity $\mathcal{L}_{\text{peak}}$ ($10^{34} \text{ cm}^{-2} \text{ s}^{-1}$)	0.9
Vertical chromaticity $\xi_y^* \approx L^*/\beta_y^*$	60 000

collision. This is known as the hourglass effect, which leads to a luminosity reduction. In the CLIC 380-GeV parameters set, there is still margin to increase luminosity by reducing the vertical beta function from $\beta_y^* = 100 \mu\text{m}$ to the same value as the bunch length, $\beta_y^* = 70 \mu\text{m}$. On the other hand, it leads to the growth of the vertical disruption parameter by approximately 20% ($D_y \sim \frac{1}{\sigma_y^*(\sigma_y^* + \sigma_x^*)}$). The initial disruption

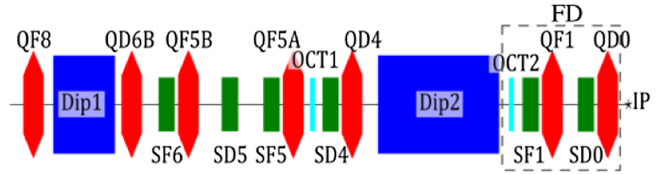


FIG. 2. Schematic layout of the CLIC FFS. Quadrupoles are shown in red, sextupoles in green, dipoles in blue, and octupoles in cyan.

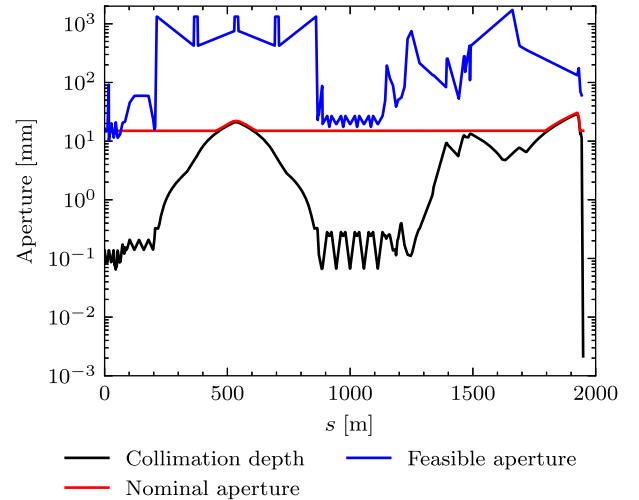


FIG. 3. Apertures of the magnets along the BDS. The black line corresponds to the aperture evaluated for the collimation depth as $\max(15\sigma_x, 55\sigma_y)$. The nominal aperture also takes into account the lower boundary of 15 mm and an additional 1.1 mm for the beam pipe thickness and possible magnet offset. The feasible aperture (blue) corresponds to the maximum aperture, which allows the pole tip field to be less than 1.5 T.

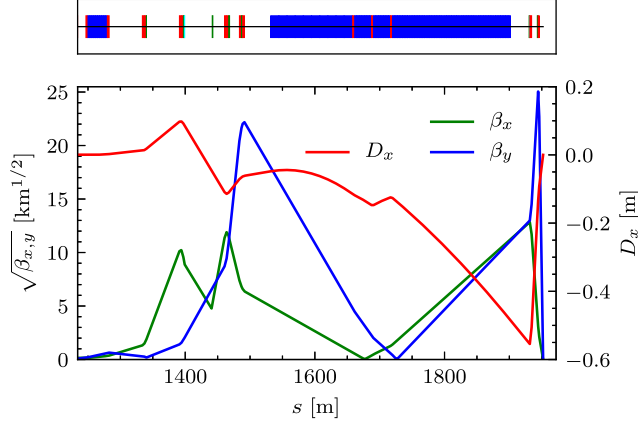


FIG. 4. Beta functions and dispersion for the new optics with $\beta_y^* = 70 \mu\text{m}$.

parameter values are $D_x = 0.24$ and $D_y = 12.5$ [14]. The large values of the disruption parameter can have a strong impact on the luminosity stability as well as the tolerances for the dynamic effects and the feedback systems.

The Twiss parameters are rematched in MAD-X [15] for the new β_y^* using the matching quadrupoles (see Fig. 4). The beam size at the IP is then matched to the linear values using the six available sextupoles, namely SD0, SF1, SD4, SF5, SD5, SF6, and two octupoles, namely OCT1 and OCT2. The sextupoles and octupoles play a key role in correcting chromatic effects in the beam. Chromaticity in this context is defined as [16]:

$$\sigma_{x,y}^{*2} = \epsilon_{x,y} \beta_{x,y}^* (1 + \xi_{x,y}^2 \delta_p^2), \quad (2)$$

where $\epsilon_{x,y}$ is the beam emittance, $\beta_{x,y}^*$ is the beta function at the IP, δ_p is the relative momentum spread of the beam, and $\xi_{x,y}$ is the chromaticity at the IP. The calculations are performed in MAD-X with PTC [17] and Mapclass [18]. Similarly to the design with $\beta_y^* = 100 \mu\text{m}$, octupoles are needed to cancel the third-order vertical aberrations. The final beam sizes are $\sigma_x^* = 143.48 \text{ nm}$ and $\sigma_y^* = 2.72 \text{ nm}$,

TABLE II. Optimized integrated strengths of the sextupoles and octupoles.

Magnet	Integrated strength	
	K2L (m^{-2})	K3L (m^{-3})
SD0	0.84	...
SF1	-0.23	...
SD4	0.55	...
SF5	0.29	...
SD5	-1.70	...
SF6	0.96	...
OCT1	...	-9.07
OCT2	...	-0.40

see Fig. 8. Required sextupole and octupole strengths are given in Table II.

Calculation of the total luminosity ($\mathcal{L}_{\text{total}}$) and peak luminosity ($\mathcal{L}_{\text{peak}}$), which only takes into account collision events with a relative energy offset not greater than 1%, is done with the particle tracking codes PLACET [19,20] and Guinea Pig [21,22]. In the transverse plane, the Gaussian distribution based on the optical parameters at the BDS entrance is used to generate the beam. In the longitudinal plane, a flattop energy profile is utilized with a 1% energy spread width. We also consider synchrotron radiation in the tracking. The luminosity evaluated for this optics is $\mathcal{L}_{\text{total}} = 1.66 \times 10^{34} \text{ cm}^{-2} \text{ s}^{-1}$ and $\mathcal{L}_{\text{peak}} = 0.96 \times 10^{34} \text{ cm}^{-2} \text{ s}^{-1}$. This new optics has increased the total luminosity by 2% and the peak luminosity by 3% (see Table VII). Furthermore, this new optics with $\beta_y^* = 70 \mu\text{m}$ has been used in luminosity tuning simulations in the presence of realistic errors performed in [23]. On average, the low β_y^* optics tunes 13% faster reaching 2.5% higher luminosity. On the other hand, the number of machines that did not reach the target luminosity of $1.65 \times 10^{34} \text{ cm}^{-2} \text{ s}^{-1}$ increased from 3.2% to 5.4% if compared to the optics with $\beta_y^* = 100 \mu\text{m}$.

III. NONLINEAR OPTIMIZATION OF FFS WITH SHORT FD

The longer L^* optics was designed by scaling up the original optics with $L^* = 4.3 \text{ m}$, where all drifts and magnet lengths were increased correspondingly to reach $L^* = 6 \text{ m}$. As a result, the length of the FFS increased from 550 to 770 m [4]. The apertures evaluated for the BDS magnets (see Fig. 3) show that almost all the quadrupoles, except for the few at the BDS entrance, respect the 1.5-T field limit. It is also valid for both QF1 and QD0 magnets, although, based on the “hybrid” design of the QD0 magnet [24], the maximum pole tip field could be approximately 2.2 T. Table III shows the FD quadrupoles settings after the reduction of the vertical IP beta function. The pole tip field for both QF1 and QD0 is way lower than 2.2 T, which allows to decrease their length. Based on this, we decrease the length of QF1 and QD0 to approximately 2.79 and 1.69 m. The advantage of the FD with shorter magnets is that it generates less chromaticity and reduces the beta-function level in the whole FFS, see Fig. 5. When the QF1

TABLE III. The key parameters of the FD quadrupoles for the optics with $\beta_y^* = 70 \mu\text{m}$.

	QF1	QD0
Magnetic length (m)	5.59	4.69
Integrated strength K1L (m^{-1})	0.076	-0.184
Aperture (mm)	27.4	27.4
Pole tip field (T)	0.23	0.68

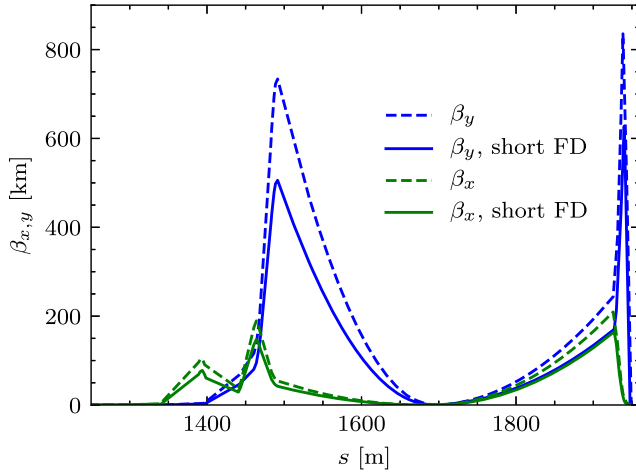


FIG. 5. Beta functions β_x and β_y along the FFS for the design with short FD (solid line) and for the original FD (dashed line) both with $\beta_y^* = 70 \mu\text{m}$.

and QD0 are shortened, their magnetic fields are increased accordingly to keep the same integrated strength. The final drift L^* is kept with length of 6 m. Optics is rematched with MAD-X, for the same IP parameters as in Sec. II.

After rematching the optics, we must ensure that the condition for simultaneous correction of horizontal chromaticity and second-order dispersion is restored. This necessitates the FD chromaticity to be similar to the upstream chromaticity. For this purpose, we scan the upstream chromaticity and match the second-order beam size for each point. As evaluated in the Appendix, the square of the minimum horizontal beam size at the IP is a quadratic function of the upstream chromaticity. We denote ξ_x^{FD} as the horizontal chromaticity generated at the IP by the FD, and ξ_x^{up} as the horizontal chromaticity generated at the IP by the elements upstream to the FD. The chromaticity difference impacting the horizontal beam size at the IP is:

$$\Delta\xi_x = \xi_x^{\text{FD}} - \xi_x^{\text{up}}. \quad (3)$$

To modify ξ_x^{up} , the distance between the section of the dipole magnets Dip2 and the FD is changed (refer to Fig. 2). In this case, FD chromaticity remains the same, while the beta-function level along the FFS is affected, which directly impacts the upstream chromaticity. For each distance change, the Twiss parameters are matched with quadrupoles, and the second-order beam size is matched using the sextupoles. Figure 6 shows the plot of the second-order horizontal beam size as a function of chromaticity difference $\Delta\xi_x$ evaluated for each distance change between Dip2 and FD. Also, Fig. 7 connects $\Delta\xi_x$ with the change in the distance between Dip2 and FD. The parabolic fit of the square of the horizontal beam size gives the optimal difference of $\Delta\xi_x \approx 47$. This is achieved by inserting an additional drift of length $\Delta L \approx 4.75$ m between Dip2 and the FD. The final settings for the sextupoles are

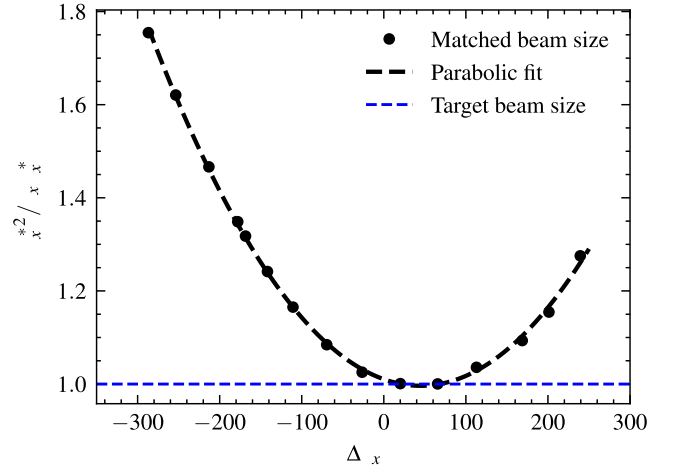


FIG. 6. The second-order horizontal beam size normalized to the linear beam size at the IP as the function of the difference between the FD and upstream chromaticity.

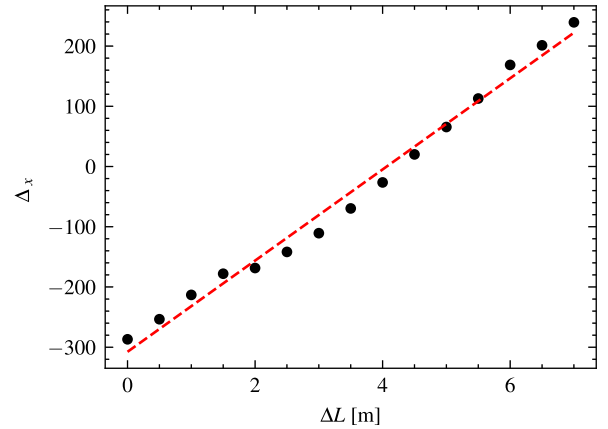


FIG. 7. Difference between the FD and upstream chromaticity as a function of the distance change between Dip2 and FD.

obtained from the fifth-order beam size matching. Table IV gives the optimal magnetic strengths of each sextupole to get the smallest beam size of $\sigma_x^* = 143.02$ nm and $\sigma_y^* = 2.63$ nm, see Fig. 8.

The larger the dispersion at the sextupole locations are, the weaker the sextupoles needed to compensate for the chromaticity and the lower the aberrations at the IP are. On the other hand, a large dispersion level requires stronger dipoles and ultimately leads to energy loss and beam emittance growth due to synchrotron radiation. These two effects have to be balanced to reach the highest luminosity.

Calculation of $\mathcal{L}_{\text{total}}$ and $\mathcal{L}_{\text{peak}}$ for this optics gives $1.66 \times 10^{34} \text{cm}^{-2} \text{s}^{-1}$ and $0.96 \times 10^{34} \text{cm}^{-2} \text{s}^{-1}$, respectively.

TABLE IV. Optimized integrated strength of the sextupoles.

Magnet	SD0	SF1	SD4	SF5	SD5	SF6
Strength K2L (m^{-2})	1.18	-0.21	0.71	-0.38	2.02	0.41

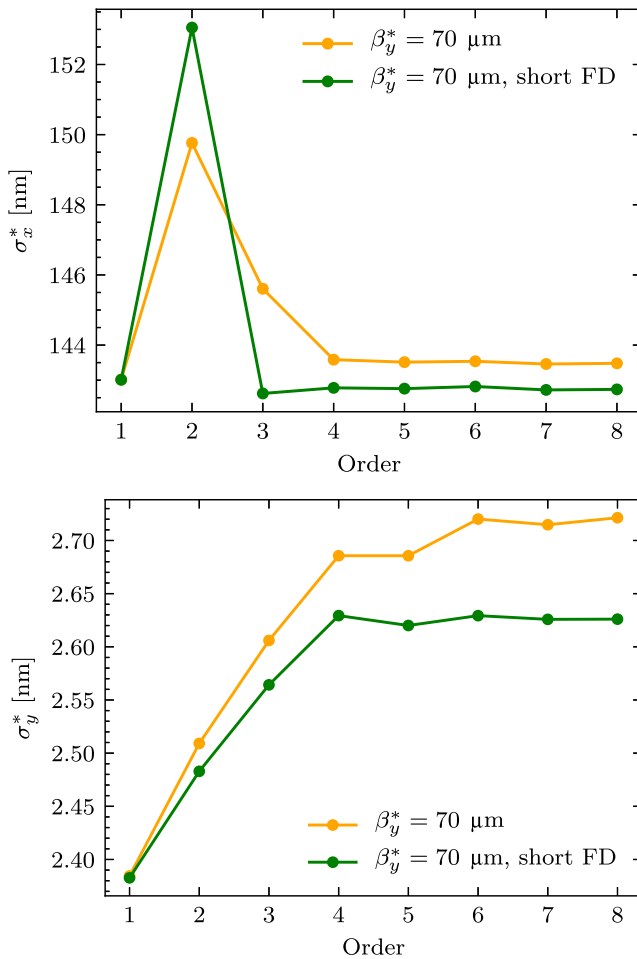


FIG. 8. Horizontal (top) and vertical (bottom) beam size at the IP as a function of the map order.

It is expected that this optics has a better energy bandwidth with respect to the other $\beta_y^* = 70 \mu\text{m}$ optics, due to the smaller vertical chromaticity.

The dispersion level is modified by scaling the bending angles of all the dipoles in the FFS. In the calculations, the dipole strengths were scanned in the relative range 0.37–1.31 of their original strength with a step of 6.25%. The dispersion profile for different scaling factors is shown in Fig. 9. For each scale factor, the sextupole settings were adjusted to optimize the beam size at the IP with MAD-X and Mapclass, and the luminosity was calculated with PLACET and Guinea Pig. Such a scan is shown in Fig. 10. One can see that the dispersion level established in the nominal design is still the optimal choice for the current optics and does not require any changes.

IV. NONLINEAR OPTIMIZATION OF FFS WITH SHORT FD AND ALTERNATIVE DISPERSION PROFILE

It has been found that by inverting the strength of one of the quadrupoles of the FFS, namely QD6B (refer to Fig. 2),

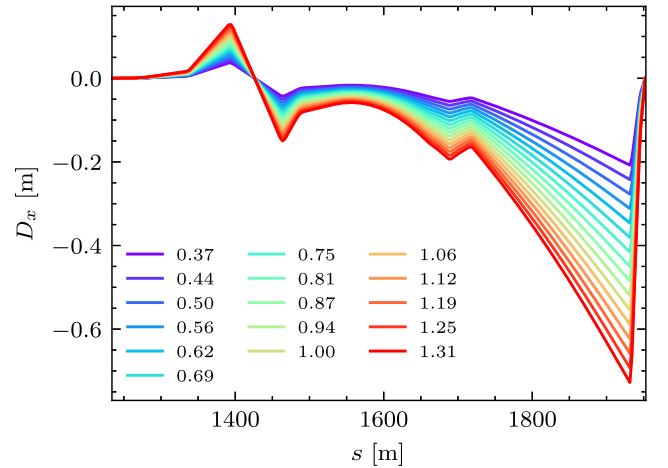


FIG. 9. Dispersion in the FFS for different scales of the bending angle of the dipoles for the optics with $\beta_y^* = 70 \mu\text{m}$ and short FD quadrupoles.

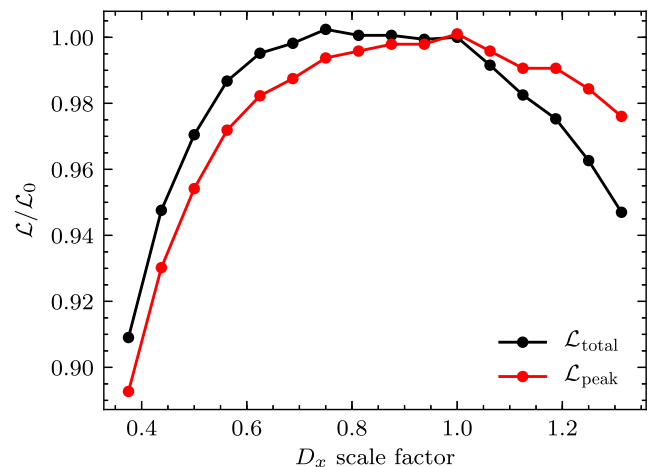


FIG. 10. Luminosity dependence of the dispersion level along the FFS for the optics with $\beta_y^* = 70 \mu\text{m}$ and short FD quadrupoles.

a new dispersion profile can be established for the FFS, see Fig. 11. In this case, the quadrupole inverts the dispersion slope, allowing larger dispersion at the FD for the same dipoles bending angles.

The optics requires the same retuning as in Sec. III, due to the new dispersion profile. An approach that was used is based on the simultaneous matching of the IP Twiss parameters and the upstream chromaticity to the given value, using the quadrupoles upstream of the FD. For each chromaticity value the second-order beam size is minimized with the sextupoles, see Fig. 12. By applying the parabolic fit, one can find the minimum, which corresponds to the chromaticity difference of $\Delta\xi_x^* \approx 171$. The sextupole settings are obtained from the numerical optimization with MAD-X and Mapclass, strengths are varied to minimize the fifth-order beam size. The beam size obtained after the

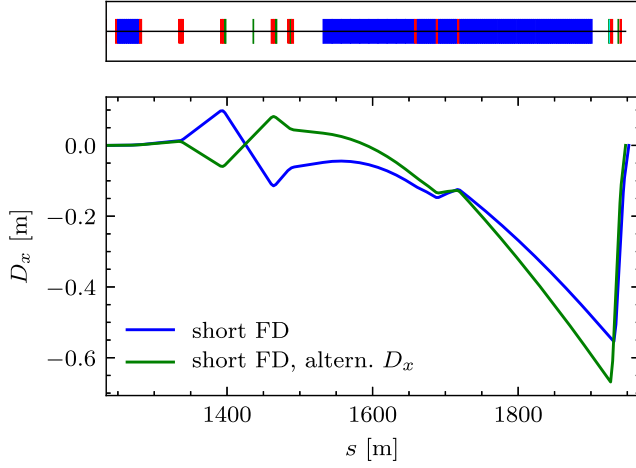


FIG. 11. Comparison between the original and the alternative dispersion profile in the FFS.

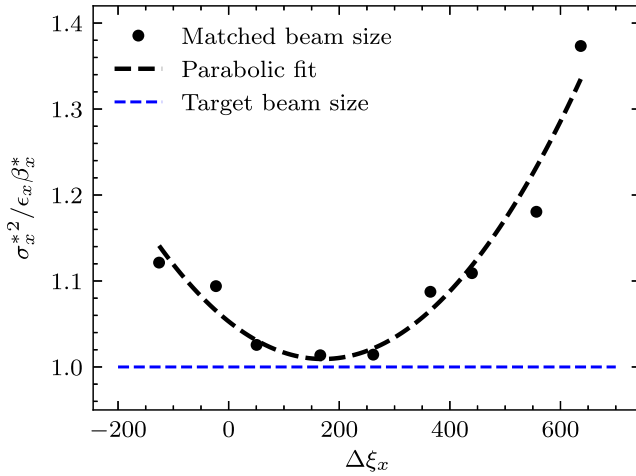


FIG. 12. The second-order horizontal beam size normalized to the linear beam size at the IP as a function of the difference between the FD and upstream chromaticities.

optimization is $\sigma_x^* = 144.31$ nm and $\sigma_y^* = 3.92$ nm and is far from the target. The beam size as a function of the order of the transfer map is given in Fig. 15 and is labeled as “before optimization.” Vertical beam size σ_y^* is large, mainly due to the third-order contributions, similar to the design in Sec. II when the octupoles are switched off. Horizontal beam size is dominated by the contributions from high-order terms.

We denote $u_{f,i} = \{x_f, x'_f, y_f, y'_f, \delta\}$ with $i \in [1, 5]$ as a particle’s coordinate at the end of the beamline. It correlates with the coordinates at the beginning in the most general form [18]:

$$u_{f,i} = \sum_{jklmn} M_{ijklmn} x_0^j x_0'^k y_0^l y_0'^m \delta_0^n, \quad (4)$$

where $u_0 \equiv \{x_0, x'_0, y_0, y'_0, \delta_0\}$ is the set of particle coordinates at the entrance. Usually, the map M_{ijklmn} is

truncated at the order q such that $j + k + l + m + n \leq q$. For horizontal and vertical coordinates we denote $M_{1ijklmn} \equiv X_{ijklmn}$ and $M_{3ijklmn} \equiv Y_{ijklmn}$, respectively. The beam size at the IP derives:

$$\sigma_{x,y}^{*2} = \sum_{\substack{jklmn \\ j'k'l'm'n'}} X(Y)_{ijklmn} X(Y)_{j'k'l'm'n'} \\ \times \int x_0^{j+j'} x_0'^{k+k'} y_0^{l+l'} y_0'^{m+m'} \delta_0^{n+n'} \rho_0 dv_0. \quad (5)$$

Integration is performed over the initial phase space, ρ_0 is the phase-space density, and dv_0 is the differential volume of the initial phase space. The map is assumed to be symplectic. Gaussian distribution is used for the transverse coordinates. In the case of CLIC, for δ , a flattop distribution is used with full width of 1%.

To analyze the IP beam size, the transfer map is truncated at fifth order. The terms inside the sum in Eq. (5) are evaluated with Mapclass and sorted in descending order. Figure 13 shows the largest contributions to the horizontal and vertical beam size. Looking at these results, several

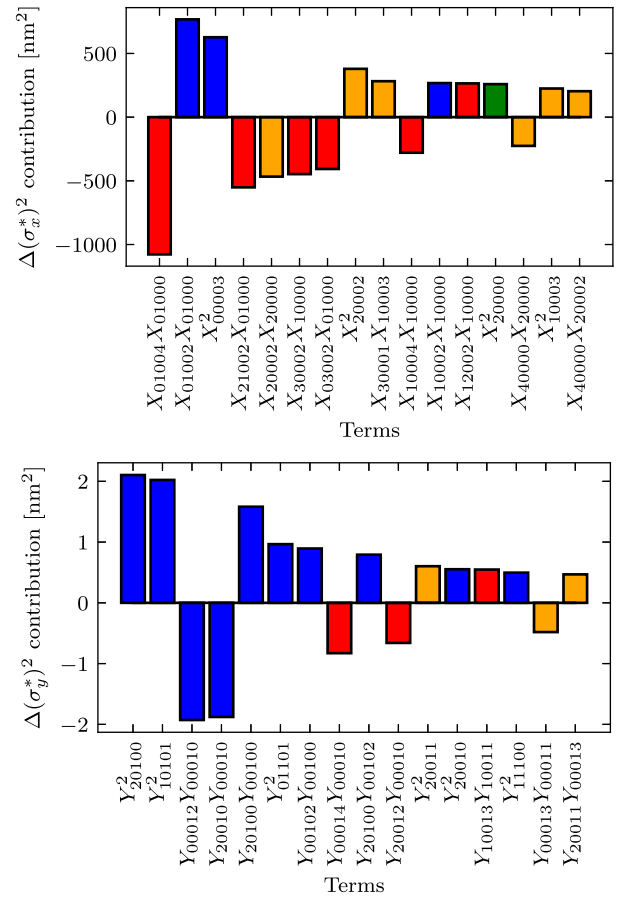


FIG. 13. The largest contributions to the square of the horizontal (top) and vertical (bottom) beam size, excluding the linear parts. The contributions of second order are shown in green, third order in blue, fourth order in orange, and fifth order in red.

outlines can be made for this design: (i) The horizontal beam size at second order is well corrected but with noticeable pure geometrical contribution from X_{20000}^2 . The third-order chromatic terms such $X_{01002}X_{01000}$ and X_{00003}^2 are dominant and are responsible for the large σ_x^* growth at third order. (ii) Horizontal beam size is reduced close to the linear value, mainly at fifth order, with the largest reduction coming from $X_{01004}X_{01000}$. (iii) Vertical beam size is almost twice the target value at fifth order. It is dominated by the third-order contributions, like the coupling terms Y_{20100}^2 and Y_{20001}^2 .

One of the main issues limiting the IP beam size is the distribution of sextupoles in the FFS and the transfer matrices between them. In this context, few improvements can be done: (i) Scan the location of SD5 to find the best position that gives the smallest beam size at the IP. For each SD5 location, the beam size at the IP is matched with the sextupoles. The results of such a scan are shown in Fig. 14. As one can see, it is possible to reduce the vertical beam size down to 2.49 nm when SD5 is shifted by 6 m further from the IP, without the need to use octupoles. (ii) Add the pair of decapoles to correct the fourth-order horizontal and vertical beam size growth. Although the fifth-order beam size is numerically optimized, the presence of fourth-order aberrations would strongly impact the beam size dependence on the energy offset and, consequently—energy bandwidth. It is suggested to put the pair of decapoles in the FD region to correct it, named DEC1 and DEC2, which are located next to the SF1 and SD0 sextupoles, respectively.

One can compare the beam sizes before and after the above optimizations, evaluated in MAD-X and Mapclass in Fig. 15. The beam size obtained after these optimizations is $142.97 \text{ nm} \times 2.52 \text{ nm}$, see Table V. To optimize the lattice in terms of luminosity at the IP and find the balance

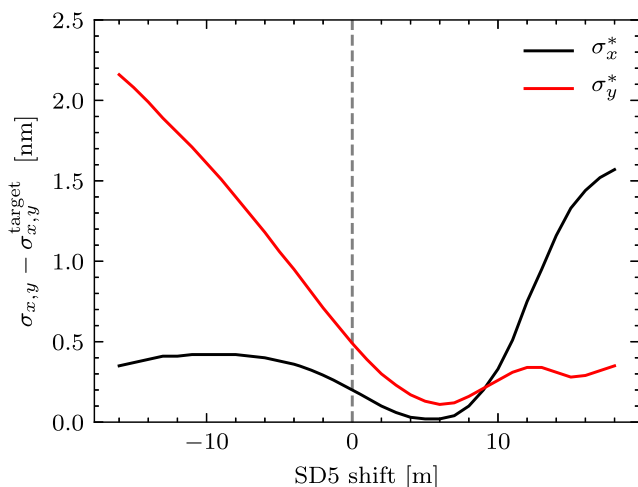


FIG. 14. Fifth-order horizontal and vertical beam sizes at the IP as a function of SD5 sextupole location. The target values are $\sigma_x^{\text{target}} = 143.00 \text{ nm}$ and $\sigma_y^{\text{target}} = 2.38 \text{ nm}$.

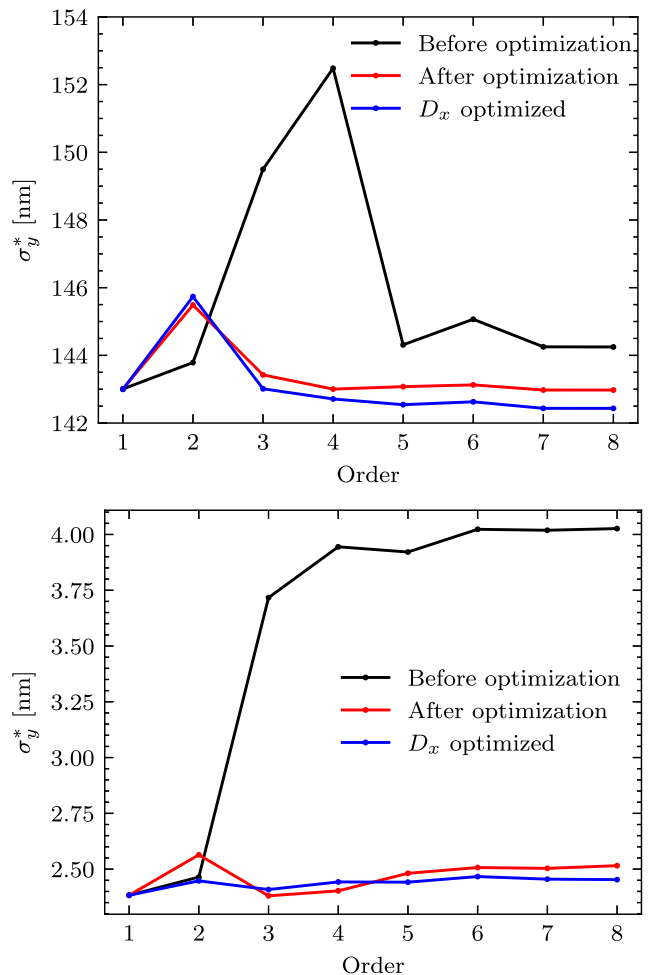


FIG. 15. Horizontal (top) and vertical (bottom) beam size at the IP before (black) and after (red) optimization. The blue line corresponds to the optics with optimized dispersion.

between emittance growth due to the synchrotron radiation and aberrations control, one needs to find the optimum dispersion scale factor. As it is shown in Table V, the vertical beam size is around 13% larger when the synchrotron radiation is considered. It might limit the total luminosity and reduce the peak luminosity at the IP. Dispersion scale factors within $\pm 50\%$ from the initial value are explored, see Fig. 16. The highest values of $\mathcal{L}_{\text{total}} = 1.74 \times 10^{34} \text{ cm}^{-2} \text{ s}^{-1}$ and $\mathcal{L}_{\text{peak}} = 1.01 \times 10^{34} \text{ cm}^{-2} \text{ s}^{-1}$ are obtained by reducing dispersion by 12.5%. The final sextupole and decapole settings are given in Table VI.

V. PERFORMANCE EVALUATION OF THE OPTICS

A. Beam size and luminosity

The beam size is calculated with MAD-X-PTC and Mapclass, including the map terms up to the eighth-order, and also is extracted from the PLACET tracking. Luminosity is calculated with Guinea Pig. The results are given in Table VII.

TABLE V. Beam size and luminosity comparisons before and after dispersion optimization for the optics with an alternative dispersion profile. Calculations with PLACET are performed including the synchrotron radiation.

	Mapclass (eighth-order map)		PLACET + Guinea-Pig			
	σ_x^* (nm)	σ_y^* (nm)	σ_x^* (nm)	σ_y^* (nm)	$\mathcal{L}_{\text{total}}$ ($10^{34} \text{ cm}^{-2} \text{ s}^{-1}$)	$\mathcal{L}_{\text{peak}}$ ($10^{34} \text{ cm}^{-2} \text{ s}^{-1}$)
Before D_x optimization	142.97	2.52	145.62	2.87	1.73	1.00
After D_x optimization	142.43	2.45	143.82	2.67	1.74	1.01

Horizontal beam size is well matched to the linear value of 143 nm for each optics. The vertical beam size of the optics with $\beta_y^* = 100 \mu\text{m}$ is at 15% larger than the largest beam size of the optics with $\beta_y^* = 70 \mu\text{m}$. Among the different designs, the optics with short FD and with a different dispersion profile provides the best aberration control, providing almost linear value of σ_y^* , see Fig. 17.

As a result, the optics with short FD and with an alternative dispersion profile provides the largest luminosity achieving a 6.7% boost of total luminosity and an 8.6% boost of peak luminosity if compared to the optics with $\beta_y^* = 100 \mu\text{m}$ and a 5% boost if compared with the rest $\beta_y^* = 70 \mu\text{m}$ optics. Estimation of the luminosity growth expectation based on the PLACET beam size approximates as 17.6%. The luminosity limiting factor due to the hourglass effect reduced from 91.6% to 86.1% for $\beta_y^* = 100 \mu\text{m}$ and $\beta_y^* = 70 \mu\text{m}$ respectively [16], which means a 5.5% difference. This gives the potential of the luminosity growth of at most 12.1%, with the actual value of 8.6%.

B. Energy bandwidth

The term energy bandwidth is used to describe the beam size or the luminosity dependence on the energy offset. In this paper, the definition from [25] is used. It is defined as the width of the region where the beam size does not grow more than 10%, compared to the on-momentum

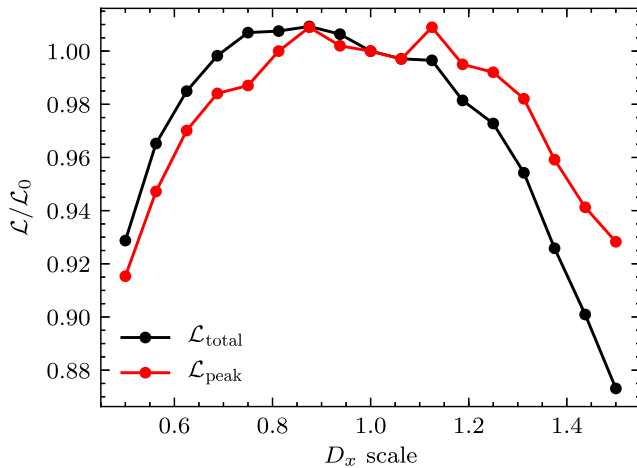


FIG. 16. Luminosity dependence of the dispersion level along the FFS for the optics with $\beta_y^* = 70 \mu\text{m}$, short FD, and the alternative dispersion profile.

beam size. For the simulation, particle tracking with PLACET is used for the beam with an energy offset in the range of $\pm 1\%$. It is worth mentioning that no energy collimation is applied so that the particle can have an energy offset larger than 1.3%. Overall, it increases the beam size and total luminosity but does not affect the peak luminosity. Figure 18 shows the calculation results for different optics. The estimated bandwidth based on it is given in Table VII.

One can see that the vertical beam size rapid growth for the off-momentum beam is responsible for the small energy bandwidth. Although it is possible to control the linear optics very well by adding the higher-order magnets, such as octupoles and decapoles, second-order beam size remains large under the presence of the energy offset. It happens due to the rapid growth of the vertical chromaticity for the off-momentum beams.

To analyze how the luminosity changes with the energy offset, the beam distributions obtained earlier are given to Guinea Pig. The results are shown in Fig. 19. One can see that the original optics with $\beta_y^* = 100 \mu\text{m}$ has the largest bandwidth for $\mathcal{L}_{\text{total}}$ mainly because of the horizontal beam size reduction for negative δp . Peak luminosity bandwidth is similar, except for the optics with different D_x profile, which is about 25% smaller.

VI. PERFORMANCE EVALUATION OF THE COLLIMATION DEPTH

CLIC's collimation section at 380 GeV was scaled down from 3 TeV and preserves the same collimation depth and

TABLE VI. Optimized integrated strength of the sextupoles and decapoles for the optics with an alternative dispersion profile.

Magnet	Strength	
	K2L (m^{-2})	K4L (m^{-4})
SD0	1.21	...
SF1	-0.29	...
SD4	0.77	...
SF5	-0.47	...
SD5	4.67	...
SF6	0.50	...
DEC1	...	-370
DEC2	...	9120

TABLE VII. Beam sizes are calculated with PLACET including synchrotron radiation and with Mapclass including transfer map terms up to the eighth order. Luminosity is calculated with Guinea Pig.

Optics	MAPCLASS				PLACET + Guinea Pig		
	σ_x^* (nm)	σ_y^* (nm)	σ_x^* (nm)	σ_y^* (nm)	$\sigma_{x,y}$ bandwidth (%)	$\mathcal{L}_{\text{total}}$ ($10^{34} \text{ cm}^{-2} \text{ s}^{-1}$)	$\mathcal{L}_{\text{peak}}$ ($10^{34} \text{ cm}^{-2} \text{ s}^{-1}$)
$\beta_y^* = 100 \mu\text{m}$	141.90	3.14	144.22	3.14	0.52	1.63	0.93
$\beta_y^* = 70 \mu\text{m}$	143.48	2.72	145.78	2.74	0.35	1.66	0.96
$\beta_y^* = 70 \mu\text{m}$, Short FD	142.74	2.63	144.72	2.71	0.42	1.66	0.96
$\beta_y^* = 70 \mu\text{m}$, Short FD + altern D_x	142.43	2.45	143.82	2.67	0.3	1.74	1.01

consists of the energy and betatron collimations in the respective order. Energy collimation removes the particles from the beam with an energy offset larger than 1.3% [5]. The betatron section aims to clean the beam halo, such that neither particles nor emitted photons hit QF1, QD0, or the inner part of the detector. Simulation studies in [6] established the optimal collimation depth of $15\sigma_x$ and $55\sigma_y$ for the 3-TeV stage. In 380 GeV lattice, the nominal

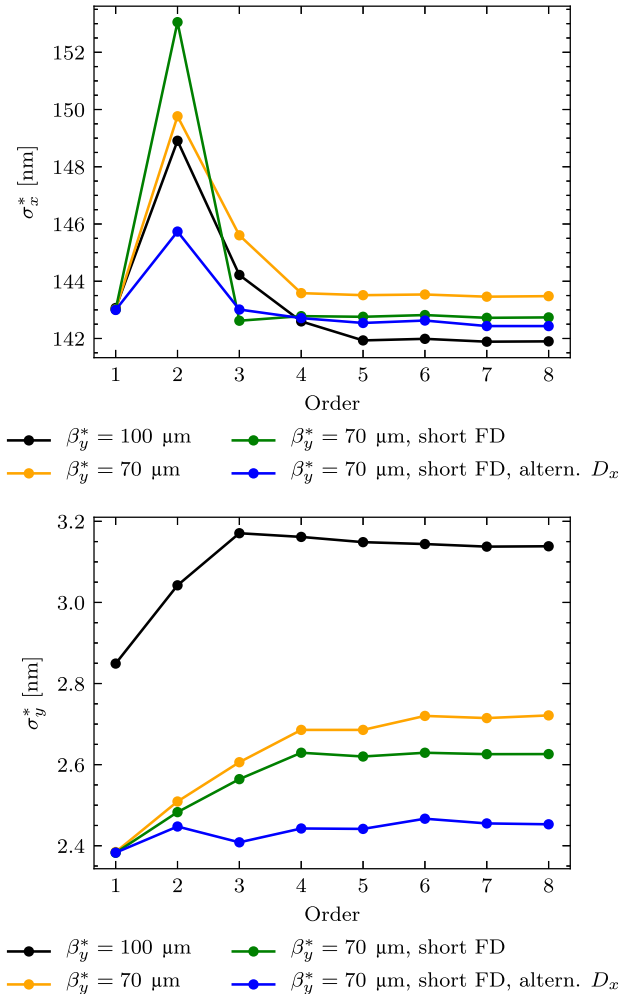


FIG. 17. Horizontal (top) and vertical (bottom) beam size as the function of the order of the map considered.

aperture is larger than 3 TeV and is comparable with the CLICdet [8] inner dimension.

Vertex detector is located in close proximity to the interaction region and has an inner radius of 31 mm, with a beam pipe of 29.4 mm inner radius. To simulate the beam halo, the monochromatic beam of the large emittance is

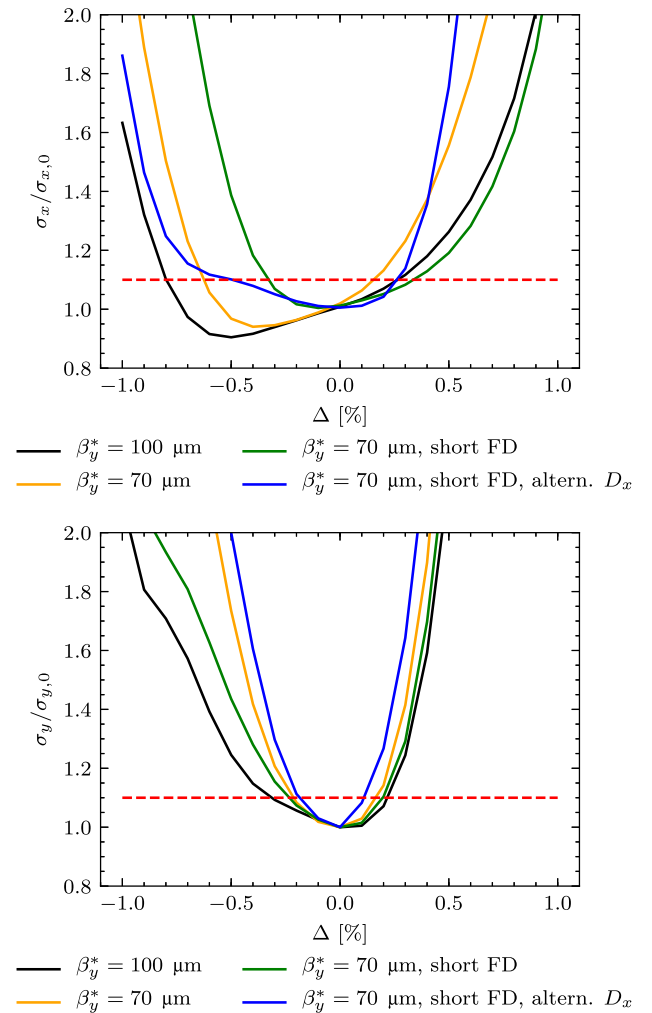


FIG. 18. Normalized horizontal (top) and vertical (bottom) beam size evaluated with PLACET including SR as the function of the energy offset. The red dashed line corresponds to a 10% beam size increase.

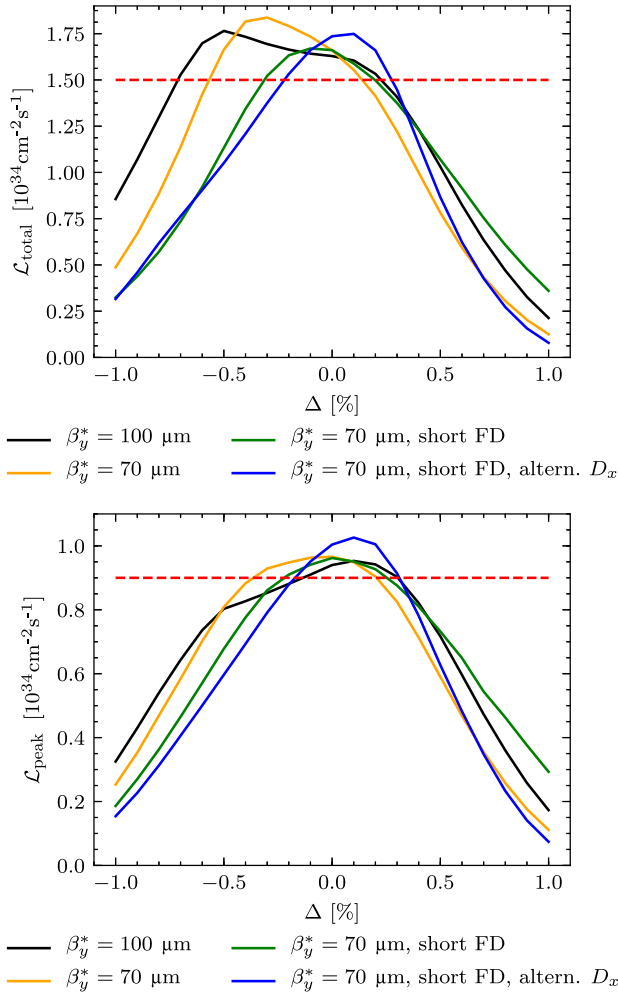


FIG. 19. Total (top) and peak (bottom) luminosity change with the energy offset normalized to the corresponding values of the on-momentum beam. Red dashed line corresponds to the nominal values from Table I.

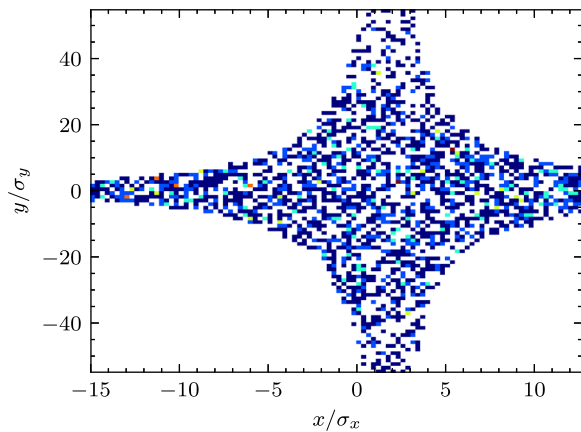


FIG. 20. Cross section of the collimated beam at the FD entrance.

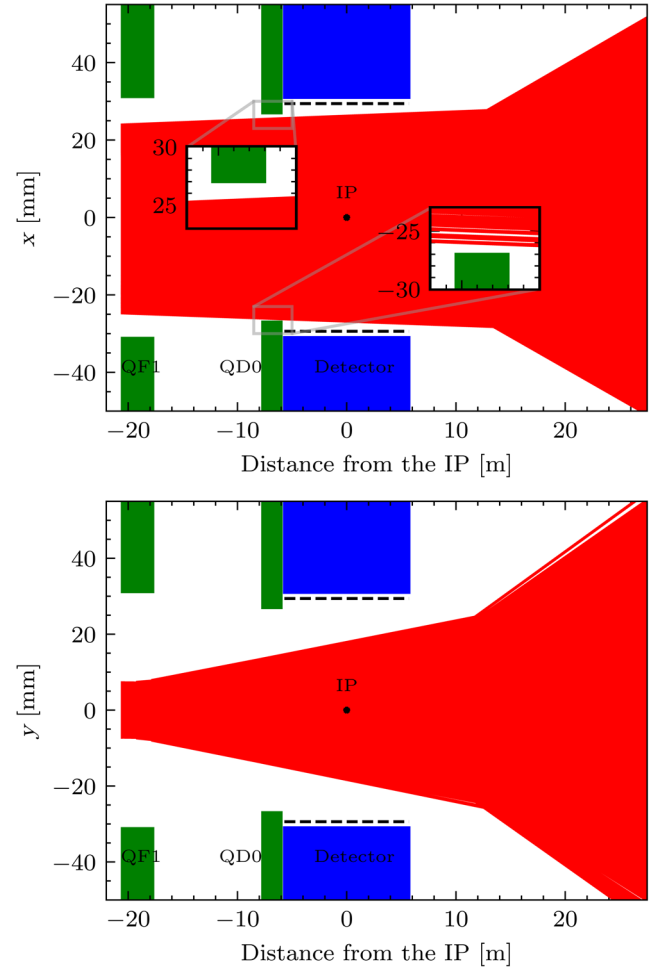


FIG. 21. Horizontal (top) and vertical (bottom) position of the emitted photons extrapolated to the entrance of the first dipole magnet in the postcollision line. The beam pipe's smallest radius around the IP is shown with the dashed line.

generated at the FFS entrance and tracked with PLACET through the FFS. Collimation cuts are applied at the FD entrance, limiting the occupied phase space to:

$$|x| < 15\sigma_x, \quad |x'| < 15\sigma_{x'}, \quad (6)$$

$$|y| < 55\sigma_y, \quad |y'| < 55\sigma_{y'}. \quad (7)$$

The beam distribution at the FD entrance is given in Fig. 20. Particles passing through QF1 and QD0 emit

TABLE VIII. The gradient and the aperture of the FD.

	QF1	QD0
Gradient (T/m)	16.3	73.7
Aperture (mm)	31.2	27.0
Pole tip field (T)	0.51	1.99

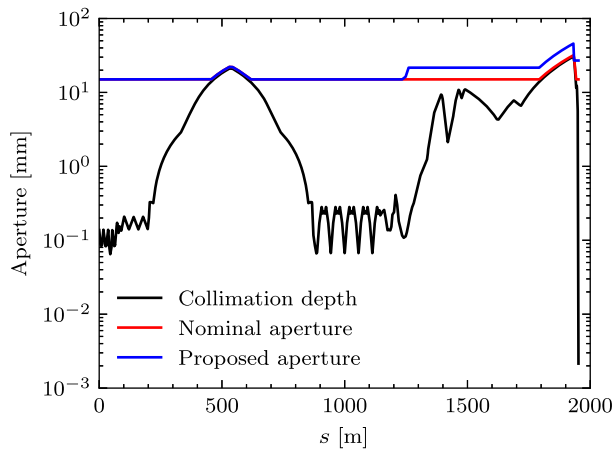


FIG. 22. Beam pipe apertures (radius) distribution along the BDS.

photons due to the synchrotron radiation. The photon emission cone's opening angle is $1/\gamma \approx 2.6 \mu\text{rad}$.

In this case, the photons are assumed to travel along the emission direction, calculated for each particle at the entrance, center, and exit of QF1 and QD0 using PLACET tracking. In Fig. 21, the photon flux is shown, including the reference apertures of the detector. One can see that photons do not hit it. QD0's aperture is adjusted based on the cone radii at their location to avoid the photons hitting the FD. We also took into account the potential quadrupoles' offsets of 0.1 mm. For QF1, it is the nominal aperture based on the collimation depth. For QD0, it is around 27.0 mm from the simulation (see Table VIII).

The photon flux emitted in QF1 and QD0 has an elliptic shape in the transverse plane with radii of around $27 \times 18 \text{ mm}^2$ at the IP location. It satisfies the requirements, as photons do not hit the detector nor the FD.

Based on the estimated aperture for the FD and including the studies of the resistive wall effects in [26], the aperture for BDS of CLIC 380 GeV is proposed, see Fig. 22. The nominal apertures, which are calculated based on the collimation depth, are increased everywhere outside the FD by 44%, and the FD aperture is set to 27 mm from the photon flux radii.

VII. CONCLUSION

Two new optics have been designed for the FFS of CLIC 380 GeV. Both of them have a vertical beta function of $70 \mu\text{m}$ and have shorter FD quadrupoles by about a factor of 2. The first optics is conceptually similar to the previous design. It provides the same luminosity as the optics with longer FD but has a 30% larger energy bandwidth and does not require octupoles. The second optics proposes the use of a different dispersion profile within the FFS. This optics features higher total and peak luminosities, which are around 5% larger than the other optics with $\beta_y^* = 70 \mu\text{m}$, but has a smaller energy bandwidth and also requires a pair

of decapoles. Considering the large luminosity gain for the same vertical beta functions, the optics with an alternative dispersion profile is preferred option for the final focus of CLIC at 380 GeV.

The collimation depth has been verified to protect the FD and the detector from the photon flux.

APPENDIX: ANALYTICAL APPROXIMATION OF THE HORIZONTAL BEAM SIZE AT THE IP

The primary source of chromaticity at the IP is the FD quadrupoles. Traditionally, the sextupoles that are put in the dispersive region are used to cancel the chromaticity. In the local chromaticity correction scheme, FD is also located in the dispersive region. This gives rise to the additional chromatic contributions to the horizontal beam size, like second-order dispersion. Correction of that requires that half of the horizontal natural chromaticity is generated upstream of the FD. In these derivations, we evaluate the minimum horizontal beam size as a function of the upstream horizontal chromaticity. Here, we do not take into account the effect of the synchrotron radiation, so the energy of each particle is assumed constant. Also, Gaussian beam density is used in the derivations.

Transformation of the horizontal coordinates through a single quadrupole, located in the no dispersion region, including the second-order transfer map terms in transfer formalism [27] is given by

$$\begin{cases} x = R_{11}x_0 + R_{12}x'_0 + T_{116}x_0\delta + T_{126}x'_0\delta \\ x' = R_{21}x_0 + R_{22}x'_0 + T_{216}x_0\delta + T_{226}x'_0\delta \end{cases} \quad (\text{A1})$$

which rewrites as:

$$\vec{x} = \hat{R} \vec{x}_0 + \begin{pmatrix} T_{116} & T_{126} \\ T_{216} & T_{226} \end{pmatrix} \vec{x}_0 \delta \equiv \hat{R} \vec{x}_0 + \hat{T}_x \vec{x}_0 \delta, \quad (\text{A2})$$

where $\vec{x} = (x, x')^T$ are the coordinates at the exit of the quadrupole, \hat{R} is the linear transfer matrix of the quadrupole, δ is the relative energy offset of the particle, $\vec{x}_0 = (x_0, x'_0)^T$ are the coordinates at the quadrupole entrance, and \hat{T}_x is the matrix of the second-order terms of the horizontal transformation. We denote \tilde{T}_x as a matrix of the second-order terms between the starting point and the IP. Considering a single quadrupole, it writes as

$$\tilde{T}_x \equiv \begin{pmatrix} \tilde{T}_{116} & \tilde{T}_{126} \\ \tilde{T}_{216} & \tilde{T}_{226} \end{pmatrix} = \hat{R}^{Q \rightarrow \text{IP}} \hat{T}_x \hat{R}^{s_0 \rightarrow Q}, \quad (\text{A3})$$

where $\hat{R}^{s_0 \rightarrow Q}$ is the transfer matrix between the starting point and the quadrupole and $\hat{R}^{Q \rightarrow \text{IP}}$ is the transfer matrix between the quadrupole and the IP. In the case of multiple quadrupoles, \tilde{T}_x is given by

$$\tilde{T}_x = \sum_i \hat{R}^{Q_i \rightarrow \text{IP}} \hat{T}_x^i \hat{R}^{s_0 \rightarrow Q_i}. \quad (\text{A4})$$

The particle's coordinate at the IP then writes:

$$\vec{x}^* \equiv (x^*, x'^*) = \hat{R}^{s_0 \rightarrow \text{IP}} \vec{x}_{s_0}^* + \tilde{T}_x \vec{x}_{s_0}^* \delta, \quad (\text{A5})$$

where $\vec{x}_{s_0}^* = (x_{s_0}, x'_{s_0})^T$ are the horizontal coordinates at the starting point, and $\hat{R}^{s_0 \rightarrow \text{IP}}$ is the transfer matrix between the starting point and the IP. Beam size at the IP writes as

$$\begin{aligned} \sigma_x^{*2} &= \epsilon_x \beta_x^* + \tilde{T}_{116}^2 \sigma_{x_{s_0}}^2 \delta_p^2 + \tilde{T}_{126}^2 \sigma_{x'_{s_0}}^2 \delta_p^2 \\ &+ 2\tilde{T}_{116} \tilde{T}_{126} \sigma_{x_{s_0} x'_{s_0}} \delta_p^2, \end{aligned} \quad (\text{A6})$$

with

$$\sigma_{x_{s_0}}^2 = \epsilon_x \beta_{x,s_0}, \quad \sigma_{x'_{s_0}}^2 = \epsilon_x \gamma_{x,s_0}, \quad \sigma_{x_{s_0} x'_{s_0}} = -\epsilon_x \alpha_{x,s_0}.$$

Here β_{x,s_0} , α_{x,s_0} , and γ_{x,s_0} are the Twiss functions at the starting point. Based on the definition in Eq. (2), one can extract the horizontal chromaticity at the IP:

$$\xi_x^2 = \tilde{T}_{116}^2 \frac{\beta_{x,s_0}}{\beta_x^*} + \tilde{T}_{126}^2 \frac{\gamma_{x,s_0}}{\beta_x^*} - 2\tilde{T}_{116} \tilde{T}_{126} \frac{\alpha_{x,s_0}}{\beta_x^*}. \quad (\text{A7})$$

In the event $\alpha_{x,s_0} = 0$, which is the case for most of the calculations with Mapclass, the equation can be simplified:

$$\xi_x^2 = \tilde{T}_{116}^2 \frac{\beta_{x,s_0}}{\beta_x^*} + \tilde{T}_{126}^2 \frac{1}{\beta_x^* \beta_{x,s_0}}. \quad (\text{A8})$$

A similar equation can also be derived for the vertical plane. In such a form, it agrees with the chromaticity definition in [28].

In the further derivations, we utilize the thin-lens approximation. So for a quadrupole, $T_{216} \approx k_L$ with k_L as the integrated strength, and the rest second-order terms are zero. We consider a single quadrupole, located at the FD phase ($\pi/2$ phase advance from the IP):

$$\hat{R}^{Q \rightarrow \text{IP}} = \begin{pmatrix} \sqrt{\frac{\beta_x^*}{\beta_x}} \alpha_x & \sqrt{\beta_x \beta_x^*} \\ -\frac{1}{\sqrt{\beta_x \beta_x^*}} & 0 \end{pmatrix}, \quad (\text{A9})$$

here β_x and α_x are the Twiss functions at the quadrupole location. Horizontal chromaticity generated by such quadrupole simplifies to

$$\xi_x^q \approx \tilde{T}_{116} \sqrt{\frac{\beta_x}{\beta_x^*}} = T_{216} R_{12}^{Q \rightarrow \text{IP}} \sqrt{\frac{\beta_x}{\beta_x^*}} = k_L \beta_x. \quad (\text{A10})$$

The entrance of the quadrupole is taken as a starting point. In the presence of the dispersion D_x at the quadrupole

location, we set $x_0 \rightarrow x_0 + D_x \delta$, and in the thin-lens approximation, Eq. (A1) transforms to

$$\begin{cases} x = R_{11}(x_0 + D_x \delta) + R_{12} x'_0 \\ x' = R_{21}(x_0 + D_x \delta) + R_{22} x'_0 + T_{216}(x_0 + D_x \delta) \delta' \end{cases} \quad (\text{A11})$$

or similarly to Eq. (A2):

$$\vec{x} = \hat{R} \vec{x}_0 + \begin{pmatrix} R_{11} \\ R_{21} \end{pmatrix} D_x \delta + \begin{pmatrix} 0 & 0 \\ T_{216} & 0 \end{pmatrix} \vec{x}_0 \delta + \begin{pmatrix} 0 \\ T_{216} D_x \end{pmatrix} \delta^2. \quad (\text{A12})$$

Particle's coordinate vector at the IP is given by $\vec{x}^* = \hat{R}^{Q \rightarrow \text{IP}} \vec{x}$. It gives the following beam size:

$$\sigma_x^{*2} = \epsilon_x \beta_x^* + \epsilon_x \beta_x^* \xi_x^{q2} \delta_p^2 + (T_{216} R_{12}^{Q \rightarrow \text{IP}} D_x)^2 3\delta_p^4, \quad (\text{A13})$$

we denote $\tilde{T}_{166}^q \equiv T_{216} R_{12}^{Q \rightarrow \text{IP}} D_x$ as the second-order dispersion generated by the quadrupole. We connect it to the chromaticity from Eq. (A10):

$$\tilde{T}_{166}^q = \sqrt{\frac{\beta_x^*}{\beta_x}} D_x \xi_x^q. \quad (\text{A14})$$

Similarly, we calculate the chromaticity and second-order dispersion generated by a single sextupole. Particle's coordinates transformation after passing through a thin sextupole in the dispersive region is given by

$$\begin{cases} x = x_0 + D_x \delta \\ x' = x'_0 + T_{211}^s (x_0 + D_x \delta)^2 + T_{233}^s y_0^2 \end{cases} \quad (\text{A15})$$

here $T_{211}^s = -k_L^s/2$, $T_{233}^s = k_L^s/2$, k_L^s is the sextupole integrated strength, and y_0 is the vertical displacement at the sextupole entrance. Horizontal coordinate at the IP, after the transformation $\hat{R}^{Q \rightarrow \text{IP}}$ writes:

$$\begin{aligned} x^* &= x_{\text{betatron}}^* + T_{211}^s R_{12}^{Q \rightarrow \text{IP}} x_0^2 + T_{233}^s R_{12}^{Q \rightarrow \text{IP}} y_0^2 \\ &+ 2T_{211}^s D_x R_{12}^{Q \rightarrow \text{IP}} x_0 \delta + T_{211}^s D_x^2 R_{12}^{Q \rightarrow \text{IP}} \delta^2. \end{aligned} \quad (\text{A16})$$

We denote

$$\begin{cases} \tilde{T}_{111}^s \equiv T_{211}^s R_{12}^{Q \rightarrow \text{IP}} = -\frac{1}{2} k_L^s \sqrt{\beta_x \beta_x^*} \\ \tilde{T}_{133}^s \equiv T_{233}^s R_{12}^{Q \rightarrow \text{IP}} = \frac{1}{2} k_L^s \sqrt{\beta_x \beta_x^*} \\ \tilde{T}_{116}^s \equiv 2T_{211}^s D_x R_{12}^{Q \rightarrow \text{IP}} = -k_L^s D_x \sqrt{\beta_x \beta_x^*} \end{cases}.$$

The terms \tilde{T}_{111}^s and \tilde{T}_{133}^s are pure geometrical contributions, which are the source of the geometrical aberrations at the IP. They can be canceled with an additional sextupole of equal strength located upstream in the dispersion-free

region. It requires $-I$ transformation between the sextupoles. According to Eq. (A7), chromaticity generated by a single sextupole is

$$\xi_x^s \approx \tilde{T}_{116}^s \sqrt{\frac{\beta_x}{\beta_x^*}} = -k_L^s D_x \beta_x. \quad (\text{A17})$$

And the second-order dispersion

$$\tilde{T}_{166}^s \equiv T_{211}^s D_x^2 \hat{R}_{12}^{Q \rightarrow \text{IP}} = \frac{1}{2} \sqrt{\frac{\beta_x^*}{\beta_x}} D_x \xi_x^s. \quad (\text{A18})$$

We construct the minimum system needed for the simultaneous correction of the horizontal chromaticity and second-order dispersion generated by the quadrupole. It requires two sextupoles, one sextupole is placed next to a quadrupole, the second is located in the upstream dispersion-free region to provide $-I$ transformation between them, see Fig. 23. Horizontal coordinate of the particle at the IP for such a system writes:

$$x^* = x_{\text{betatron}}^* + (\tilde{T}_{116}^q + \tilde{T}_{116}^s) x_0 \delta + (\tilde{T}_{166}^q + \tilde{T}_{166}^s) \delta^2. \quad (\text{A19})$$

Also, we introduce the additional chromaticity ξ_x^{up} , generated by the quadrupoles upstream in the dispersion-free region. Combining Eqs. (A10), (A14), (A17), and (A18), horizontal beam size at the IP evaluates

$$\sigma_x^{*2} = \epsilon_x \beta_x^* + \epsilon_x \beta_x^* (\xi_x^{\text{up}} + \xi_x^q + \xi_x^s)^2 \delta_p^2 + 3 \frac{\beta_x^*}{\beta_x} D_x^2 (\xi_x^q + \xi_x^s / 2)^2 \delta_p^4. \quad (\text{A20})$$

One can see that to cancel the second-order dispersion, we need $\xi_x^s = -2\xi_x^q$. Therefore to also cancel chromaticity, we need an additional contribution with value $\xi_x^{\text{up}} = \xi_x^q$.

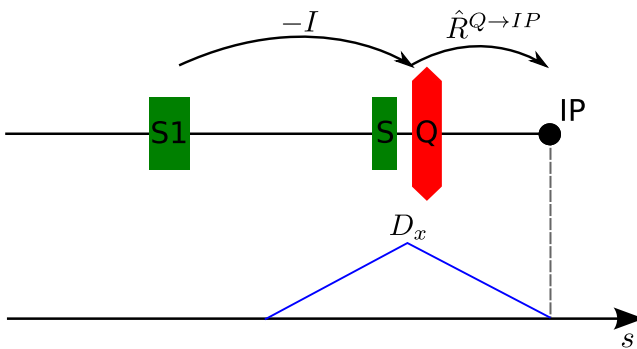


FIG. 23. Minimum scheme required for the correction of the horizontal chromaticity and second-order dispersion in the FFS.

When the optics is not tuned well, the natural chromaticity generated upstream is not optimal $\xi_x^{\text{up}} = \xi_x^q + \Delta \xi_x$. We search for new amount of the chromaticity generated by the sextupole $\xi_x^s = -2\xi_x^q + \Delta \xi_x^s$ to minimize the horizontal beam size by solving $\frac{d}{d\Delta \xi_x^s} \sigma_x^{*2} = 0$. We get

$$\Delta \xi_x^s = -\frac{\Delta \xi_x}{1 + \frac{3}{4} \frac{D_x^2}{\beta_x \epsilon_x} \delta_p^2}, \quad (\text{A21})$$

$$\begin{aligned} \frac{\sigma_x^2}{\epsilon_x \beta_x^*} &= 1 + (\Delta \xi_x + \Delta \xi_x^s)^2 \delta_p^2 + \frac{3}{4} \frac{D_x^2}{\beta_x \epsilon_x} (\Delta \xi_x^s)^2 \delta_p^4 \\ &= 1 + \frac{\Delta \xi_x^2 \delta_p^2}{1 + \frac{4}{3} \frac{\epsilon_x \beta_x}{D_x^2 \delta_p^2}}. \end{aligned} \quad (\text{A22})$$

When the dispersion at upstream sextupole S1 (refer to Fig. 23) is nonzero, it also contributes to the beam size via the chromaticity and second-order dispersion at the IP:

$$\begin{aligned} \sigma_x^{*2} &= \epsilon_x \beta_x^* + \epsilon_x \beta_x^* (\xi_x^{\text{up}} + \xi_x^q + \xi_x^s + \xi_x^{s1})^2 \delta_p^2 \\ &\quad + 3 \frac{\beta_x^*}{\beta_x} D_x^2 \left(\xi_x^q + \xi_x^s / 2 - \xi_x^{s1} / 2 \frac{D_x^{s1}}{D_x} \right)^2 \delta_p^4, \end{aligned} \quad (\text{A23})$$

where D_x^{s1} is the dispersion at upstream sextupole and $\xi_x^{s1} = -k_{s,L1} \beta_x D_x^{s1}$ is the chromaticity it generates. The minus sign in the second-order dispersion contribution appears due to the $-I$ transformation. The strength of the upstream sextupole is set $k_L^{s1} = k_L^s$ to cancel the geometrical aberrations. The optimal upstream chromaticity evaluates as

$$\xi_x^{\text{up}} = \xi_x^q \frac{1 + D_x^{s1}/D_x}{1 - D_x^{s1}/D_x}. \quad (\text{A24})$$

It requires the sextupoles to be set to produce the following chromaticities:

$$\xi_x^s = -\frac{2\xi_x^q}{1 - \left(\frac{D_x^{s1}}{D_x}\right)^2}, \quad \xi_x^{s1} = -\frac{2\xi_x^q}{1 - \left(\frac{D_x^{s1}}{D_x}\right)^2} \frac{D_x^{s1}}{D_x}, \quad (\text{A25})$$

leading to the full cancellation of the above aberrations. In the presence of the additional upstream chromaticity $\Delta \xi_x$, cancellation of the geometrical aberrations does not strictly correspond to the minimum beam size. One has to include the geometrical and chromogeometrical terms to evaluate the minimum beam size. Given the fact that in CLIC FFS design, there are six sextupoles, we also need to include the impact from the rest of the sextupoles located at large β_x locations. In the current design, we have one additional sextupole, namely SF6, referred to as S2 in Fig. 24. It is located at dispersive region with D_x^{s2} dispersion and at 2π phase advance from the FD. Similarly

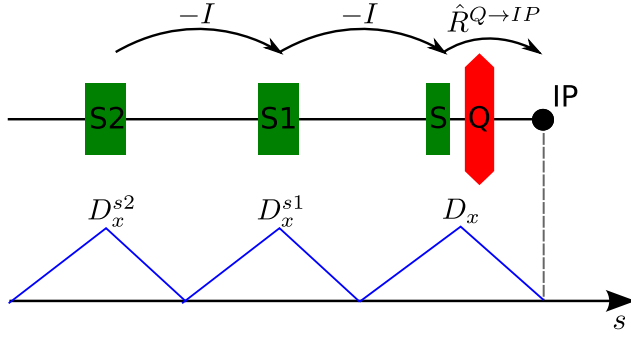


FIG. 24. The scheme of the correction of the horizontal aberrations used in CLIC FFS.

to Eq. (A19), we evaluate the horizontal coordinate at the IP, including the geometrical terms:

$$\begin{aligned}
 x^* &= x_{\text{betatron}}^* + \left(\tilde{T}_{116}^q + \tilde{T}_{116}^s + \tilde{T}_{116}^{s1} + \tilde{T}_{116}^{s2} \right) x_0 \delta \\
 &+ \left(\tilde{T}_{166}^q + \tilde{T}_{166}^s - \tilde{T}_{166}^{s1} + \tilde{T}_{166}^{s2} \right) \delta^2 \\
 &- \left(\tilde{T}_{111}^s - \tilde{T}_{111}^{s1} + \tilde{T}_{111}^{s2} \right) x_0^2 \\
 &+ \left(\tilde{T}_{133}^s - \tilde{T}_{133}^{s1} + \tilde{T}_{133}^{s2} \right) y_0^2. \quad (\text{A26})
 \end{aligned}$$

We connect the pure geometrical terms of the sextupoles with the chromaticity of the corresponding magnet as follows:

$$\tilde{T}_{111}^s = -\tilde{T}_{133}^s = \frac{\xi_x^s}{2D_x} \sqrt{\frac{\beta_x^*}{\beta_x}}. \quad (\text{A27})$$

When horizontal chromaticity generated upstream differs from the value given in Eq. (A24) by $\Delta\xi_x$, we adjust the amount of chromaticity generated by the sextupoles S and S1 by $\Delta\xi_x^s$ and $\Delta\xi_x^{s1}$ with respect to Eq. (A25). At the same time, we want to find the optimal settings for S2 sextupole, $\xi_x^{s2} = -k_L^s \beta_x D_x^{s2}$ to minimize the horizontal beam size at the IP. The horizontal beam size for such a system, based on Eq. (A26) with upstream chromaticity $\xi_x^{\text{up}} = \xi_x^q \frac{1+D_x^1/D_x}{1-D_x^1/D_x} + \Delta\xi_x$ and including Eq. (A27) writes:

$$\begin{aligned}
 \sigma_x^{*2} &= \epsilon_x \beta_x^* + \epsilon_x \beta_x^* \left(\Delta\xi_x + \Delta\xi_x^s + \Delta\xi_x^{s1} + \xi_x^{s2} \right)^2 \delta_p^2 \\
 &\times 3 \frac{\beta_x^*}{\beta_x} D_x^2 \left(\frac{\Delta\xi_x^s}{2} - \frac{\Delta\xi_x^{s1}}{2} \frac{D_x^{s1}}{D_x} + \frac{\xi_x^{s2}}{2} \frac{D_x^{s2}}{D_x} \right)^2 \delta_p^4 \\
 &+ \frac{3\beta_x^*}{4\beta_x} \left(\frac{\Delta\xi_x^s}{D_x} - \frac{\Delta\xi_x^{s1}}{D_x^{s1}} + \frac{\xi_x^{s2}}{D_x^{s2}} \right)^2 \left[(\epsilon_x \beta_x)^2 + (\epsilon_y \beta_y)^2 \right] \\
 &+ \frac{\beta_x^*}{\beta_x} \left(\frac{\Delta\xi_x^s}{D_x} - \frac{\Delta\xi_x^{s1}}{D_x^{s1}} + \frac{\xi_x^{s2}}{D_x^{s2}} \right) \\
 &\times \left(\frac{\Delta\xi_x^s}{2} - \frac{\Delta\xi_x^{s1}}{2} \frac{D_x^{s1}}{D_x} + \frac{\xi_x^{s2}}{2} \frac{D_x^{s2}}{D_x} \right) D_x \delta_p^2 (\epsilon_y \beta_y - \epsilon_x \beta_x). \quad (\text{A28})
 \end{aligned}$$

The minimum is found by solving the following system of equations:

$$\begin{cases} \frac{\partial}{\partial \Delta\xi_x^s} \sigma_x^{*2} = 0 \\ \frac{\partial}{\partial \Delta\xi_x^{s1}} \sigma_x^{*2} = 0 \\ \frac{\partial}{\partial \xi_x^{s2}} \sigma_x^{*2} = 0. \end{cases} \quad (\text{A29})$$

One can use $\vec{\xi} = (\Delta\xi_x^s, \Delta\xi_x^{s1}, \xi_x^{s2})^T$ to simplify Eq. (A28) to the following form:

$$\sigma_x^{*2} = \epsilon_x \beta_x^* + \epsilon_x \beta_x^* \left(\Delta\xi_x + \sum_{i=1}^3 \xi_i \right)^2 \delta_p^2 + \sum_{i=1}^3 \sum_{j=i}^3 A_{ij} \xi_i \xi_j, \quad (\text{A30})$$

where A_{ij} are the terms one gets after comparing Eqs. (A30) and (A28). Derivatives evaluate as

$$\begin{aligned}
 \frac{\partial}{\partial \xi_l} \sigma_x^{*2} &= 2\epsilon_x \beta_x^* \left(\Delta\xi_x + \sum_{i=1}^3 \xi_i \right) \delta_p^2 \\
 &+ \sum_{i=1}^3 \sum_{j=i}^3 A_{ij} (\delta_{il} \xi_j + \delta_{jl} \xi_i), \quad (\text{A31})
 \end{aligned}$$

where δ_{ij} is Kronecker delta. By introducing the Heaviside step function \mathcal{H} , with $\mathcal{H}(0) = 1$, we rewrite the sum:

$$\begin{aligned}
 \frac{\partial}{\partial \xi_l} \sigma_x^{*2} &= 2\epsilon_x \beta_x^* \delta_p^2 \Delta\xi_x \\
 &+ \sum_{i=1}^3 \xi_i \left\{ 2\epsilon_x \beta_x^* \delta_p^2 + A_{il} [\mathcal{H}(i-l) + \mathcal{H}(l-i)] \right\}. \quad (\text{A32})
 \end{aligned}$$

In this format, the solution of Eq. (A29) simplifies to

$$\hat{M} \vec{\xi} = \Delta\xi_x \vec{b}, \quad \vec{\xi} = (\Delta\xi_x^s, \Delta\xi_x^{s1}, \xi_x^{s2})^T, \quad (\text{A33})$$

where \hat{M} and \vec{b} are the matrix and vector estimated depending on the configuration of the sextupoles. The solution is proportional to $\Delta\xi_x$, which leads to the quadratic dependence of σ_x^{*2} on $\Delta\xi_x$, similarly to Eq. (A22). This property is used to find the optimal upstream chromaticity for different optics designs in this paper.

- [1] M. Aicheler, P. Burrows, M. Draper, T. Garvey, P. Lebrun, K. Peach *et al.*, A Multi-TeV Linear Collider based on CLIC technology: CLIC conceptual design report, CERN, Geneva, Report No. CERN-2012-007, 2012.
- [2] R. Tomás, Overview of the Compact Linear Collider, *Phys. Rev. ST Accel. Beams* **13**, 014801 (2010).

- [3] M. J. Boland *et al.* (CLIC and CLICdp Collaborations), Updated baseline for a staged Compact Linear Collider, CERN, Geneva, Report No. CERN-2016-004, 2016.
- [4] F. Plassard, Optics optimization of longer L^* beam delivery system designs for CLIC and tuning of the ATF2 final focus system at ultra-low β^* using octupoles, Ph.D. thesis, Université Paris-Saclay, 2018.
- [5] J. Resta-Lopez, D. Angal-Kalinin, B. Dalena, J. Fernandez-Hernando, F. Jackson, D. Schulte, A. Seryi, and R. Tomás, Status report of the baseline collimation system of CLIC. Part I, [arXiv:1104.2426](https://arxiv.org/abs/1104.2426).
- [6] J. Resta-Lopez, D. Angal-Kalinin, B. Dalena, J. Fernandez-Hernando, F. Jackson *et al.*, Status report of the baseline collimation system of CLIC. Part II, [arXiv:1104.2431](https://arxiv.org/abs/1104.2431).
- [7] P. Raimondi and A. Seryi, Novel Final Focus Design for Future Linear Colliders, *Phys. Rev. Lett.* **86**, 3779 (2001).
- [8] N. Alipour Tehrani, J. Blaising, B. Cure, D. Dannheim, F. Duarte Ramos *et al.*, CLICdet: The post-CDR CLIC detector model, CERN, Geneva, Technical Report No. CLICdp-Note-2017-001, 2017.
- [9] F. Plassard, A. Latina, E. Marin, R. Tomás, and P. Bambade, Quadrupole-free detector optics design for the Compact Linear Collider final focus system at 3 TeV, *Phys. Rev. Accel. Beams* **21**, 011002 (2018).
- [10] F. Plassard, P. Bambade, A. Latina, E. Marín, D. Schulte, and R. Tomás, Beam delivery system optimization for CLIC 380 GeV, in *Proceedings of 8th International Particle Accelerator Conference, Copenhagen, Denmark, 2017* (JACoW, Geneva, Switzerland, 2017), mOPIK100.
- [11] A. Pastushenko, Beam optics calculations for CLIC, Master's thesis, Université Paris-Saclay, 2018.
- [12] J. Tanabe, Iron dominated electromagnets: Design, fabrication, assembly and measurements, SLAC, Stanford, CA, Technical Report No. SLAC-R-754, 2005.
- [13] W. Herr and B. Muratori, Concept of luminosity, in *Proceedings of CERN Accelerator School and DESY Zeuthen: Accelerator Physics* (CERN Yellow Reports, Zeuthen, Germany, 2003), pp. 361–377.
- [14] D. Schulte, Beam-beam effects in Linear Colliders, ICFA Beam Dyn. Newslett. **69**, 237 (2016), <https://inspirehep.net/literature/1507584>.
- [15] H. Grote and F. Schmidt, MAD-X: An upgrade from MAD8, CERN Report No. CERN-AB-2003-024, 2003.
- [16] A. W. Chao, K. H. Mess, M. Tigner, and F. Zimmermann, *Handbook of Accelerator Physics and Engineering* (World Scientific, Singapore, 2013), 2nd ed.
- [17] F. Schmidt, E. Forest, and E. McIntosh, Introduction to the polymorphic tracking code: Fibre bundles, polymorphic Taylor types and “Exact tracking”, CERN, Geneva, Technical Report No. CERN-SL-2002-044-AP, KEK-REPORT-2002-3, 2002.
- [18] R. Tomás, Nonlinear optimization of beam lines, *Phys. Rev. ST Accel. Beams* **9**, 081001 (2006).
- [19] PLACET (Program for Linear Accelerator Correction and Efficiency Tests), https://abpcomputing.web.cern.ch/codes/codes_pages/Placet/.
- [20] D. Schulte, PLACET: A program to simulate drive beams, in *Proceedings of the European Particle Accelerator Conference, Vienna, 2000* (EPS, Geneva, 2000).
- [21] D. Schulte, Beam-beam simulations with Guinea-Pig, CERN, Geneva, Technical Report No. CLIC-Note-387, 1999.
- [22] D. Schulte, Study of electromagnetic and hadronic background in the interaction region of the TESLA Collider, Ph.D. thesis, Hamburg University, 1997.
- [23] J. Ögren, A. Latina, R. Tomás, and D. Schulte, Tuning the Compact Linear Collider 380 GeV final-focus system using realistic beam-beam signals, *Phys. Rev. Accel. Beams* **23**, 051002 (2020).
- [24] M. Modena, CLIC project R&D studies: The magnet system for the 3 TeV, CERN, Geneva, Technical Report No. CLIC-Note-1074, 2017.
- [25] T. O. Raubenheimer, NLC ZDR: Zero order design report for the NEXT Linear Collider (Volume 1), SLAC National Accelerator Laboratory Technical Report No. SLAC-R-474, 2018.
- [26] D. Arominski, A. Latina, and D. Schulte, Resistive wall effects in the CLIC beam delivery system, in *Proceedings of the 10th International Particle Accelerator Conference, Melbourne, 2019* (JACoW, Geneva, Switzerland, 2019), mOPGW071.
- [27] K. L. Brown, A first- and second-order matrix theory for the design of beam transport systems and charged particle spectrometers, SLAC, Stanford, CA, Technical Report No. SLAC-75, 1971.
- [28] E. Marin Lacoma, Design and higher order optimisation of final focus systems for Linear Colliders, Ph.D. thesis, Universitat Politècnica de Catalunya, Institut de Tècniques energètiques, 2012.